Supporting Information to

Poleward shift in the Southern Hemisphere westerly winds synchronous with the deglacial rise in CO_2

William R. Gray[1]*, Casimir de Lavergne[2], Robert C. Jnglin Wills[3,4], Laurie Menviel[5,6], Paul Spence[6,7,8], Mark Holzer[9], Masa Kageyama[1], Elisabeth Michel[1]

[1]Laboratoire des Sciences du Climat et de l'Environnement (LSCE/IPSL), Université Paris-Saclay, Gif-sur-Yvette, France
[2]LOCEAN Laboratory, Sorbonne Université-CNRS-IRD-MNHN, Paris, France
[3]Institute for Atmospheric and Climate Science, ETH Zurich, 8092 Zurich, Switzerland
[4]Department of Atmospheric Sciences, University of Washington, Seattle, WA 98195, USA
[5]Climate Change Research Centre, University of New South Wales, NSW 2052 Sydney, Australia
[6]The Australian Centre for Excellence in Antarctic Science, University of Tasmania, Hobart, Tasmania 7001, Australia
[7]Institute for Marine and Antarctic Studies, University of Tasmania, Hobart, Australia
[8]Australian Antarctic Partnership Program, University of Tasmania, Hobart, Australia
[9]School of Mathematics and Statistics, University of New South Wales, NSW 2052 Sydney, Australia

*correspondence to: william.gray@lsce.ipsl.fr

Table of contents

Other supporting information not included in this file

Table S1   New and compiled Southern Ocean planktic foraminiferal $\delta^{18}O$ data: original data reference, core name, latitude (°N), longitude (°E), water depth (m), species (gr = *G. ruber*, gb = *G. bulloides*, np = *N. pachyderma*), sediment depth (cm), age (ka), $\delta^{18}O$ (per mil, VPDB).

Table S2 ΔLat_{SST} [ALL, Indian-Pacific, Atlantic] (°) and ΔLat_{wind} (°) from 10 to 20 ka, with 68 and 95% CI.

Table S3 ΔLat_{SST} [Indian-Pacific] (°), ΔLat_{wind} (°), wind strength (N/m²), zonal-mean zonal-wind stress at 60°S [$\tau_{u,60S}$] (N/m²), and northward Ekman transport at 60°S (Sv) from 6.5 to 20 ka, with 68 and 95% CI.

Using $\delta^{18}O_{calcite}$ to track the SST front latitude

Although $\delta^{18}O_{calcite}$ is a function of both temperature and $\delta^{18}O_{water}$, at the basin scale the effect of temperature dominates over $\delta^{18}O_{water}$. Using the Southern Ocean salinity-$\delta^{18}O_{water}$ relationship of (LeGrande & Schmidt, 2006) a meridional salinity difference of greater than 25 PSU would be required to equal the meridional temperature changes across the basin (Fig. S1). As no physical mechanism exists to drive such changes, the meridional pattern of $\delta^{18}O_{calcite}$ will always be dominated by temperature. Furthermore, the meridional profile of $\delta^{18}O_{water}$ is itself closely linked to the meridional profile of SST in the Southern Ocean (Fig.S1d,e): the SST gradient shapes the meridional trend in near-surface moisture (via the Clausius-Clapeyron relation), hence the meridional trend in evaporation minus precipitation caused by downgradient moisture transport (Siler et al., 2018), and ultimately the $\delta^{18}O_{water}$ trend (e.g., Akhoudas et al., 2023). Consequently, the $\delta^{18}O_{water}$ profile is expected to remain tightly coupled to, and shift in tandem with, the SST profile of the Southern Ocean. There is no mechanism to drive large shifts in the $\delta^{18}O_{water}$ profile independent of shifts in the SST profile. While changes in sea ice are expected to drive changes in salinity across the Southern Ocean, there is little fractionation of $\delta^{18}O$ during the formation of sea ice (Paren & Potter, 1984; Strain & Tan, 1993). Meridional profiles of $\delta^{18}O_{calcite}$ thus allow us to identify and track the SST front latitude (Gray et al., 2020).

Seasonality of planktic foraminifera

$\delta^{18}O$ records measured on species of foraminifera with different temperature/seasonal habitats at the same (or nearby) mid-latitude sites, indicate the impacts of seasonality on the reconstruction are likely to be small. Foraminiferal species with different habitat temperature preferences (*G. bulloides* and *N. pachyderma*, Lombard et al., 2011) show very similar Holocene-LGM changes (compare circles and triangles on Fig. 1a). The leave-one-out analysis (Fig. 2d-g) shows that records of *G. bulloides* and *N. pachyderma* $\delta^{18}O$ are both contributing highly to the ΔLat_{SST} reconstruction. Besides, the relatively warm temperature preference of *G. bulloides* (the dominant species in the mid-latitudes) means that global SST cooling during the LGM would shift the annual SST distribution further away from its preferred habitat temperature, shifting its seasonal bias further towards the summer and minimising the degree of cooling it records. This would tend to reduce the anomalous mid-latitude cooling at the LGM, and would make our ΔLat_{SST} (and thus ΔLat_{wind}) reconstruction conservative.

Suitability of the southeast Pacific data

The southeast Pacific has a bimodal pattern of meridional SST gradient (Fig. 1a). The northern maximum near 40°S partially overlaps with the core of the wind belt, whereas the southern maximum near 58°S is controlled by Drake Passage's effect on ocean circulation and is spatially offset from the core wind belt. Only the northern maximum is sampled by the present compilation of cores and tracked in our analysis (Fig. 1; Fig S2). The model ensemble indicates the latitude of the SST front located north of the Drake Passage is linked to the latitude of the winds (Fig. S5). Hence inclusion of the southeast Pacific data in our reconstruction is justified. We note that excluding the southeast Pacific data from our analysis results in a similar time series of the wind latitude to that shown in Figs. 6 and 7, however the uncertainties for the LGM increase by 1.4° at the 95% CI.

MOM5-SIS-Wombat results

As a result of the equatorward shifted winds the surface DIC concentration decreases by 13 mmol/m^3 south of 60°S (Fig. 12), thus leading to a surface $pCO2_{DIC}$ decrease of 25 ppm, which is partly compensated by a decrease of surface alkalinity of 8.6 mmol/m^3 (Delta $pCO2_{alk}$ = +14 ppm). The solubility contribution to $pCO2_{sol}$ is negligible south of 60°S.

While the model also displays an increase in Antarctic sea ice extent in the Perturbed experiment (not shown), likely an impact of the reduction in upwelling of relatively warm deepwaters, the decrease in CO_2 flux out of the polar ocean is associated with decreased surface ocean pCO_2 rather than increased air-sea disequilibria. Hence, changes in wind-driven carbon supply, rather than sea ice driven disequilibria, cause the reduction in CO_2 outgassing from the polar Southern Ocean. Furthermore, the CO_2 flux anomalies are largely decoupled from the sea ice anomalies around the basin. Both pCO_2 and CO_2 flux anomalies are, however, clearly linked to changes in Ekman divergence. As a result of shifted winds, the DIC concentration increases in the Southern Ocean below the sub-surface south of 60°S by about 10 mmol/m^3, and DIC increases throughout the deep ocean below 1.5km (Figs. 11 and 12), even if the magnitude of the increase is small due to the short duration of the experiment. The increase in upwelling between 60°S and 50°S leads to a DIC increase in the top 2 km in that region, but results in a DIC decrease in the intermediate depths throughout the ocean north of 35°S (Figs. 11 and 12). These DIC changes are accompanied by similar changes in remineralised nitrogen, and inverse changes in dissolved O_2 (Figs. 11 and 12).

Preformed nutrient calculation

Extrapolating the initial changes in endmember preformed NO_3 (N_{pre}, given in mmol/m^3) based on the relative volume of the ocean they represent (V) we can broadly estimate the magnitude of CO_2 change implied by the initial changes in endmember preformed nitrate:

We take the Southern Ocean endmember as an average through the water column between 60-80°S, and the North Atlantic endmember as an average through the water column between 60-70°N in the Atlantic. In the control run $N_{pre}\_SO\_ctr$ = 22.12 and $N_{pre}\_NA\_ctr$ = 8.5. Global mean N_{pre} in the control run (N_{pre}_ctr) is 15.45. Using the global mean and endmember values we calculate the volumetric contribution of the Southern Ocean endmember (V_{SO}) as 0.51 and the North Atlantic endmember (V_{NA}) as 0.49. Total nitrate (N_{tot}) is 33.84 mmol/m^3 such that globally averaged N* in the control run is 54%.

After 125 years of the Perturbed experiment N_{pre} in both the endmembers decreases: $N_{pre}\_SO\_125$ = 20.31 and $N_{pre}\_NA\_125$ = 7.3. Assuming the same volumetric contributions as the control experiment, we calculate the expected change in global mean N_{pre} in the Perturbed run (N_{pre}_EQSH) as,

$N_{pre}\_EQSH = V_{SO}*N_{pre}\_SO\_125+V_{NA}*N_{pre}\_NA\_125$ = 13.9, equivalent to a globally averaged N* value of 59%. Based on the initial changes in N_{pre} within the endmember regions we would thus expect a global mean N* increase of ~5% in the Perturbed experiment relative to the Control, once these anomalies had propagated through the deep ocean.
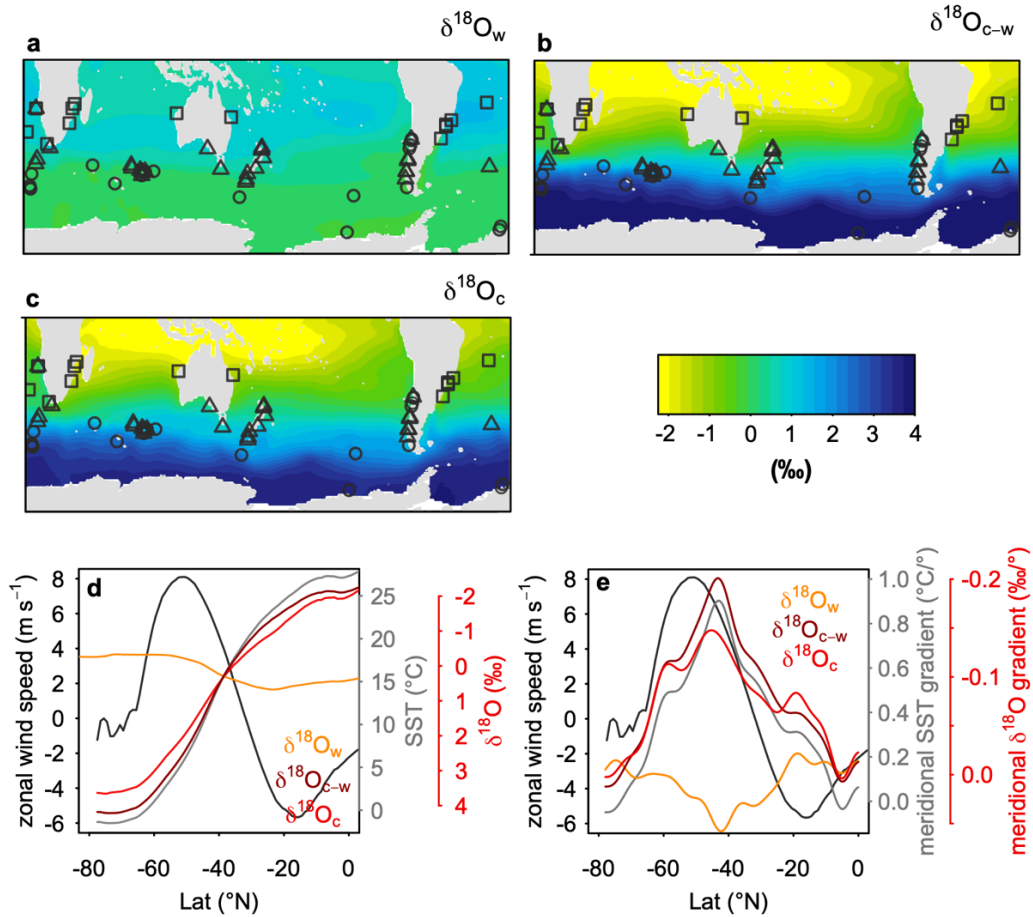
Fig. S1. **Climatological δ¹⁸O**. Surface climatological **(a)** $\delta^{18}O_{water}$ (LeGrande & Schmidt, 2006), **(b)** $\delta^{18}O_{calcite-water}$ (calculated using Boyer et al., 2013; Kim & O'Neil, 1997), and **(c)** $\delta^{18}O_{calcite}$ (note, colour scale is the same for all panels). Symbols show location of core sites and species of planktic foraminifera (circles = *N. pachyderma*, triangles = *G. bulloides*, squares = *G. ruber*). **(d)** Zonal-mean climatological $\delta^{18}O_{water}$, $\delta^{18}O_{calcite-water}$, and $\delta^{18}O_{calcite}$ at the surface (as shown on Fig. 1b), near-surface zonal wind speed (Kalnay et al., 1996), and sea surface temperature (SST) (Boyer et al., 2013). **(e)** Meridional gradients of zonal-mean surface $\delta^{18}O_{water}$, $\delta^{18}O_{calcite-water}$, $\delta^{18}O_{calcite}$ and SST. Wind speed as in (d). Note the peak gradients in $\delta^{18}O_{water}$, $\delta^{18}O_{calcite}$ and SST are almost exactly colocalised, illustrating the tight coupling of their meridional patterns.
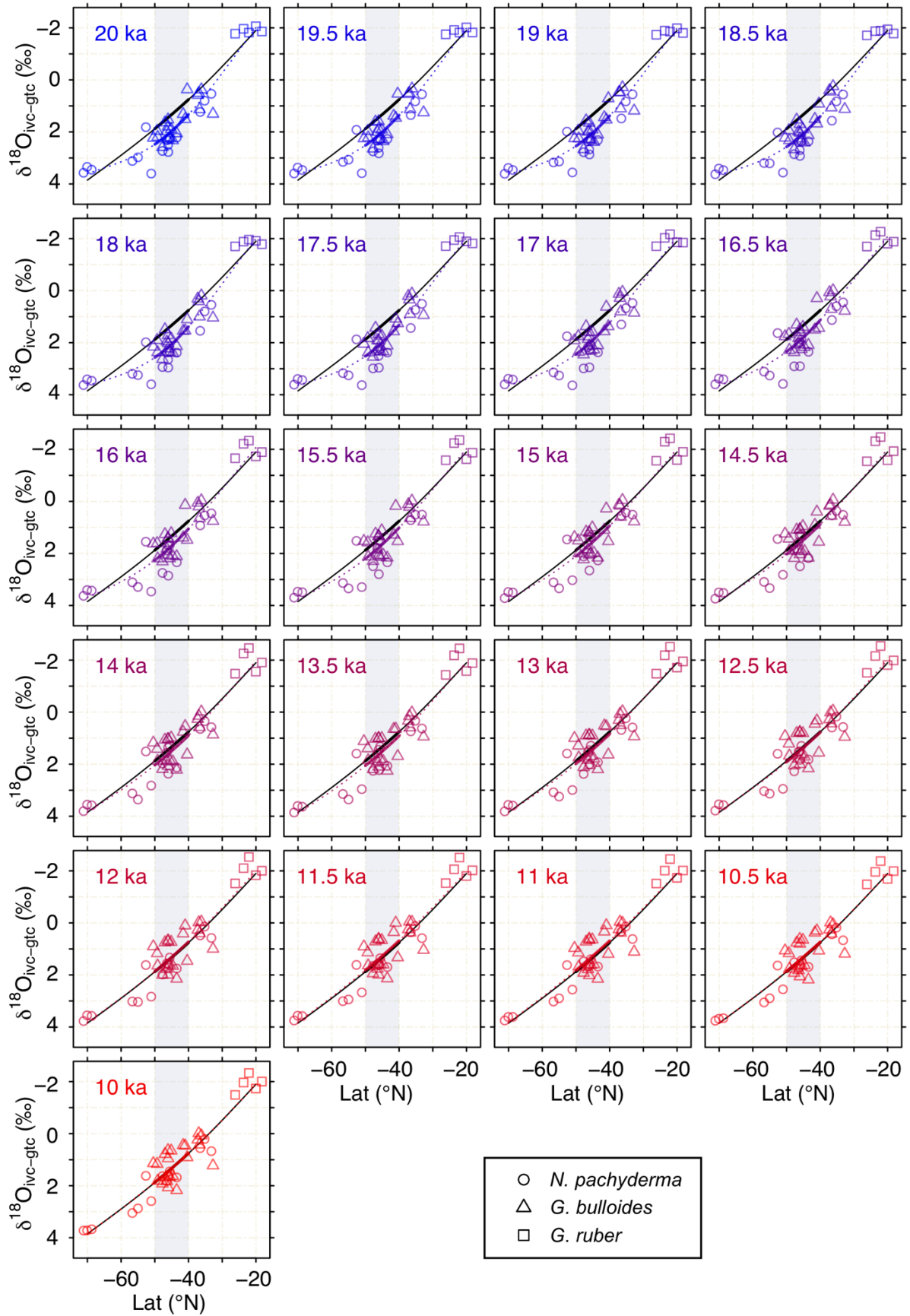
Fig. S2. Indian-Pacific meridional δ¹⁸O profiles. Indian-Pacific meridional $\delta^{18}O_{ivc\text{-}gtc}$ data with GAM fits at 500-year time steps. The GAM fit at 10 ka is shown in black. The grey box is the window in which ΔLat_{SST} is calculated and the thick lines show the portion of the curves falling within this window.

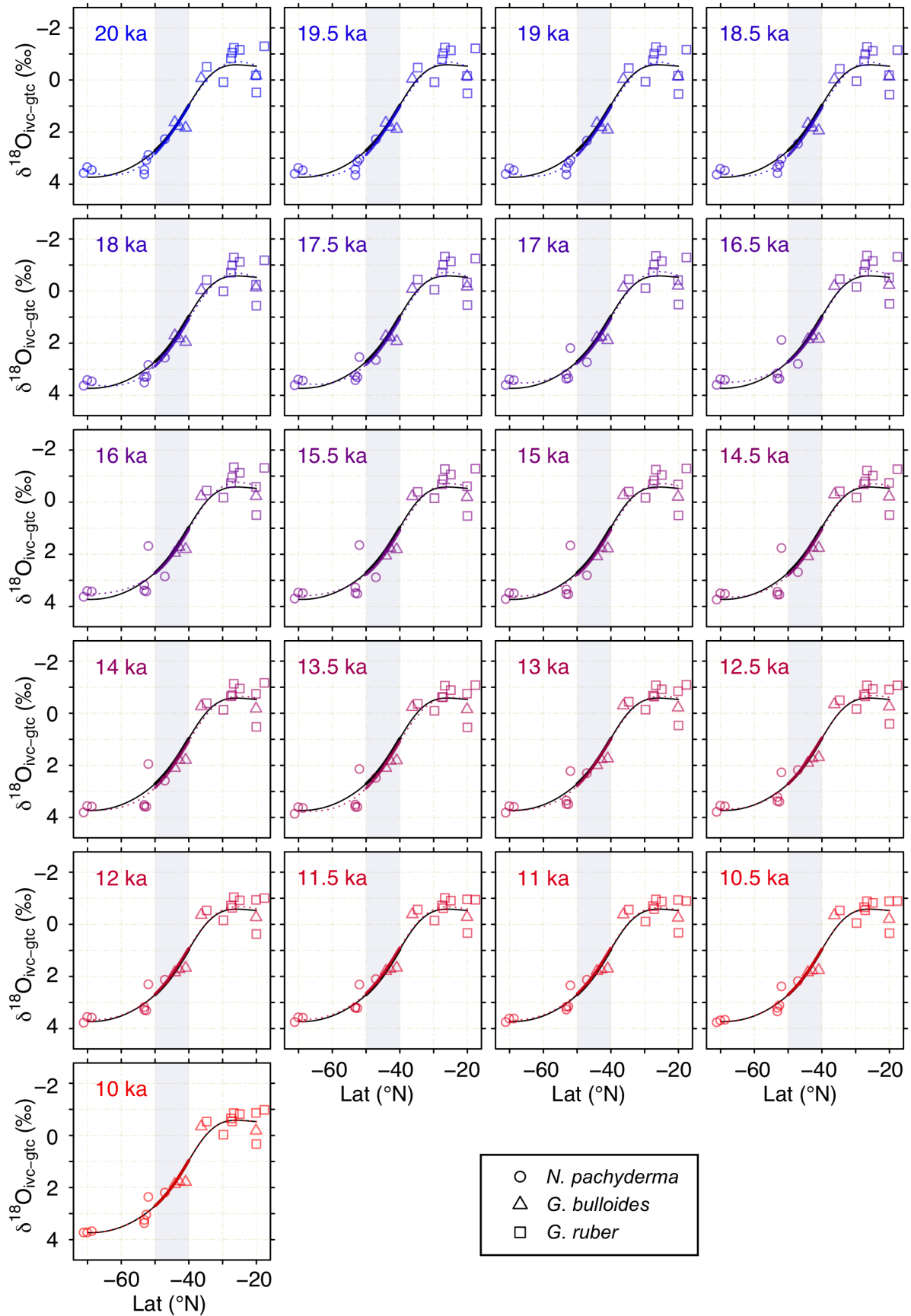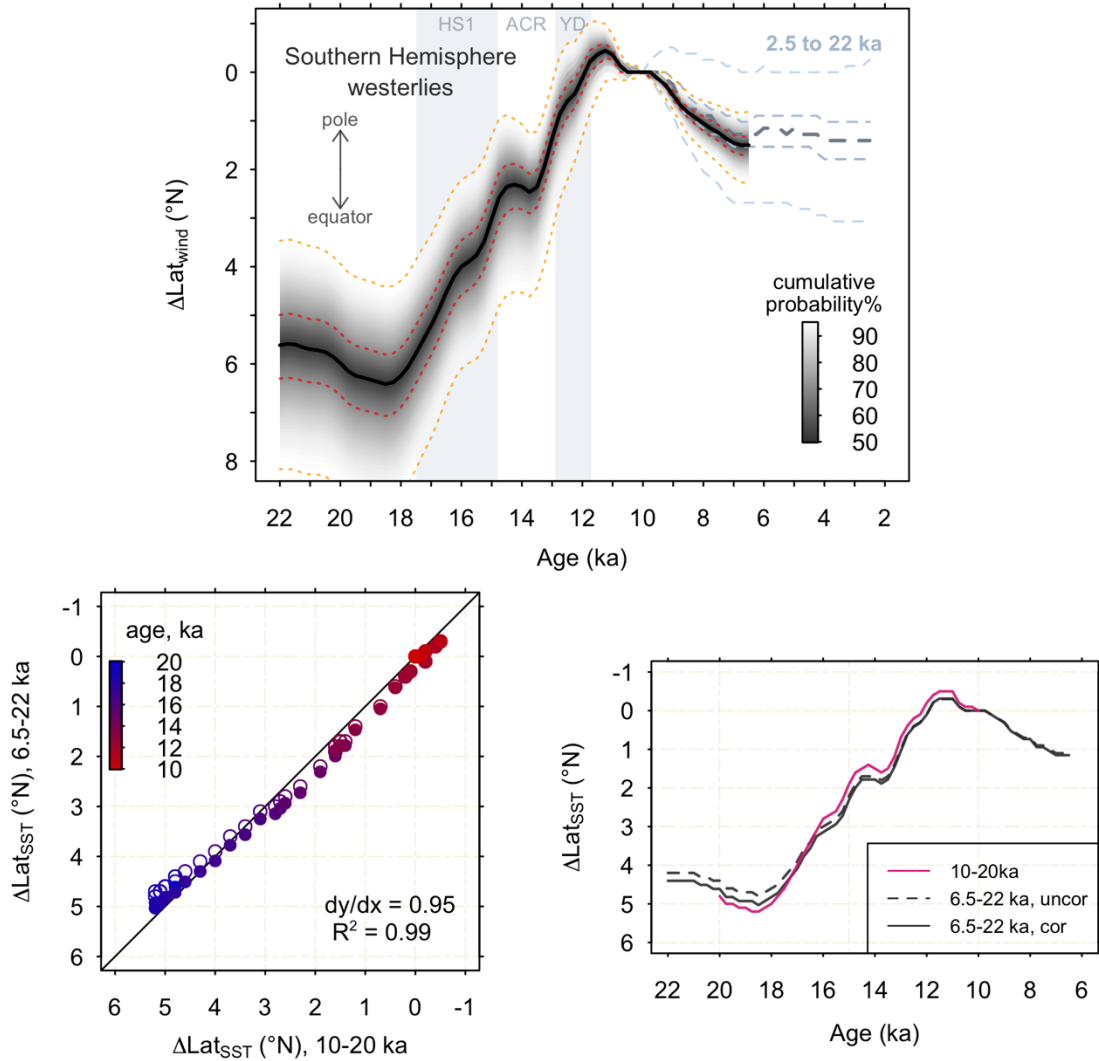**Fig. S3. Atlantic meridional δ^18O profiles.** As figure above, but for the Atlantic.

Fig. S4. 22-6.5 ka analysis. (top) Changes in the wind latitude (ΔLat_{wind}) over 22-6.5 ka. The higher uncertainties compared to the 20-10 ka reconstruction is due to the lower number of sites than span this interval. The 5th, 32nd, 50th, 68th, and 95th percentiles are indicated. The grey dashed line shows the same analysis extended to 2.5 ka; while the uncertainties are very large due to the limited number of cores than span this interval, the results suggest little change in the position of the wind latitude during the Holocene. The displayed uncertainties in ΔLat_{wind} account for uncertainty in the relationship between the SST-front latitude and wind latitude due to variations across the model ensemble (Methods) but omit possible structural uncertainties in the representation of this relationship by the models. **(bottom)** Comparison of reconstructed Indian-Pacific ΔLat_{SST} using the 10-20 ka subset and 6.5-22 ka subset of cores. Open circles and the dashed grey curve correspond to the 6.5-22 ka reconstruction uncorrected; filled circles and solid grey line correspond to the 6.5-22 ka reconstruction with a 1/0.95 correction applied (see Methods). The pink curve shows the 10-20 ka reconstruction.
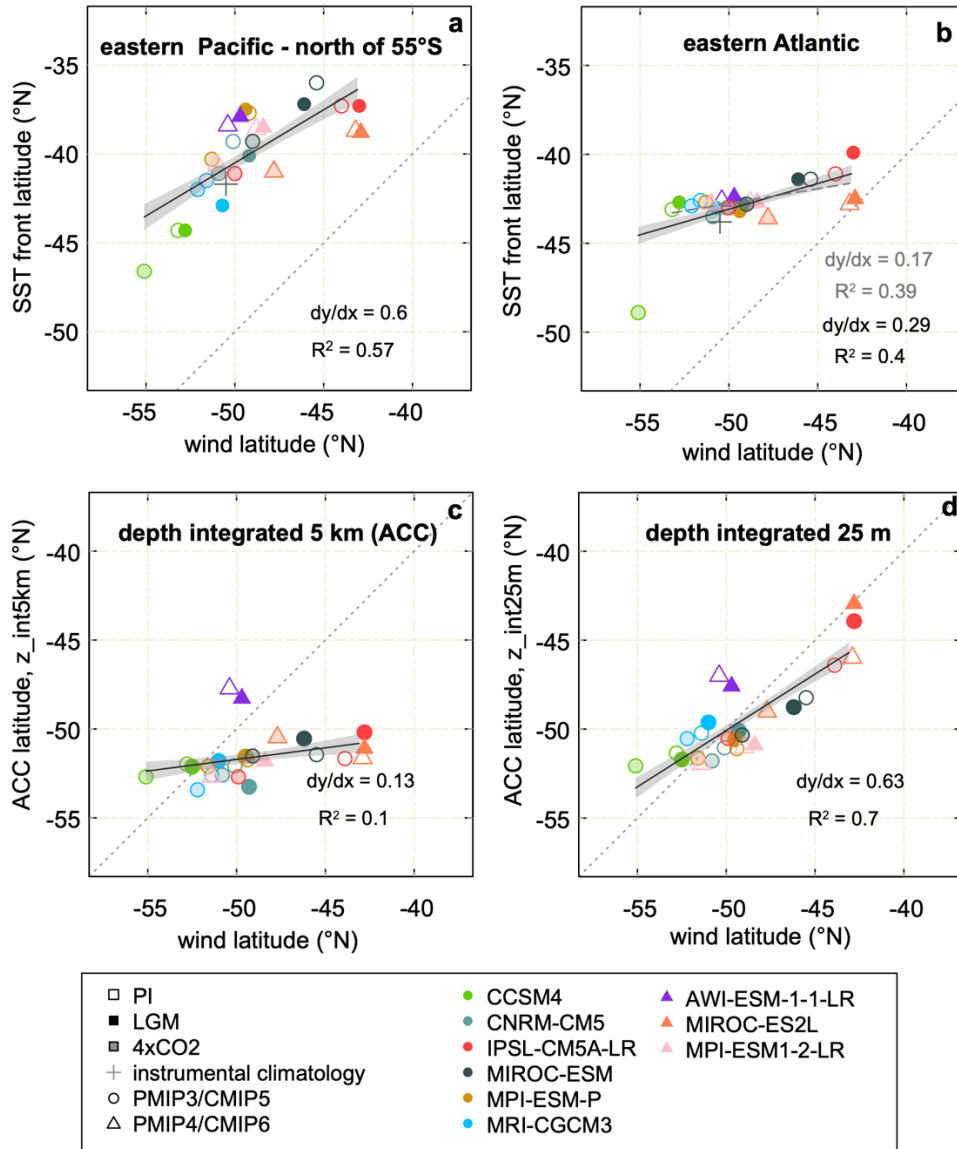
Fig. S5. PMIP3/4 and CMIP5/6 ensemble. (a) Relationship between the wind latitude and SST front latitude in the model ensemble across the eastern Pacific north of 55°S (i.e. along the coast of South America). **(b)** As (a) but for the eastern Atlantic sector, where the vast majority of the mid-latitude sites in the Atlantic are located. Dashed grey line shows regression excluding CCSM4 4xCO$_2$ simulation. The weak relationship might owe to bathymetric constraints on the latitude of the confluence of warm Indian Ocean waters and colder Southern Ocean waters south of Africa. Note, as the coupling mechanism underlying our approach is hemispheric in scale, the relationships shown in (a) and (b) are aids for interpretation only and are not used to derive changes in wind latitude. **(c,d)** Relationship between the wind latitude and the latitude of peak zonal oceanic flow in the Southern Ocean. The latitude of peak zonal flow is calculated by taking the zonal mean of the latitude of maximum depth-integrated zonal velocity. The depth integration is carried out over **(c)** the upper 5 km (i.e. full depth integration to locate the ACC), and **(d)** the upper 25m (locating the surface jet). Dotted lines show 1:1 relationship.
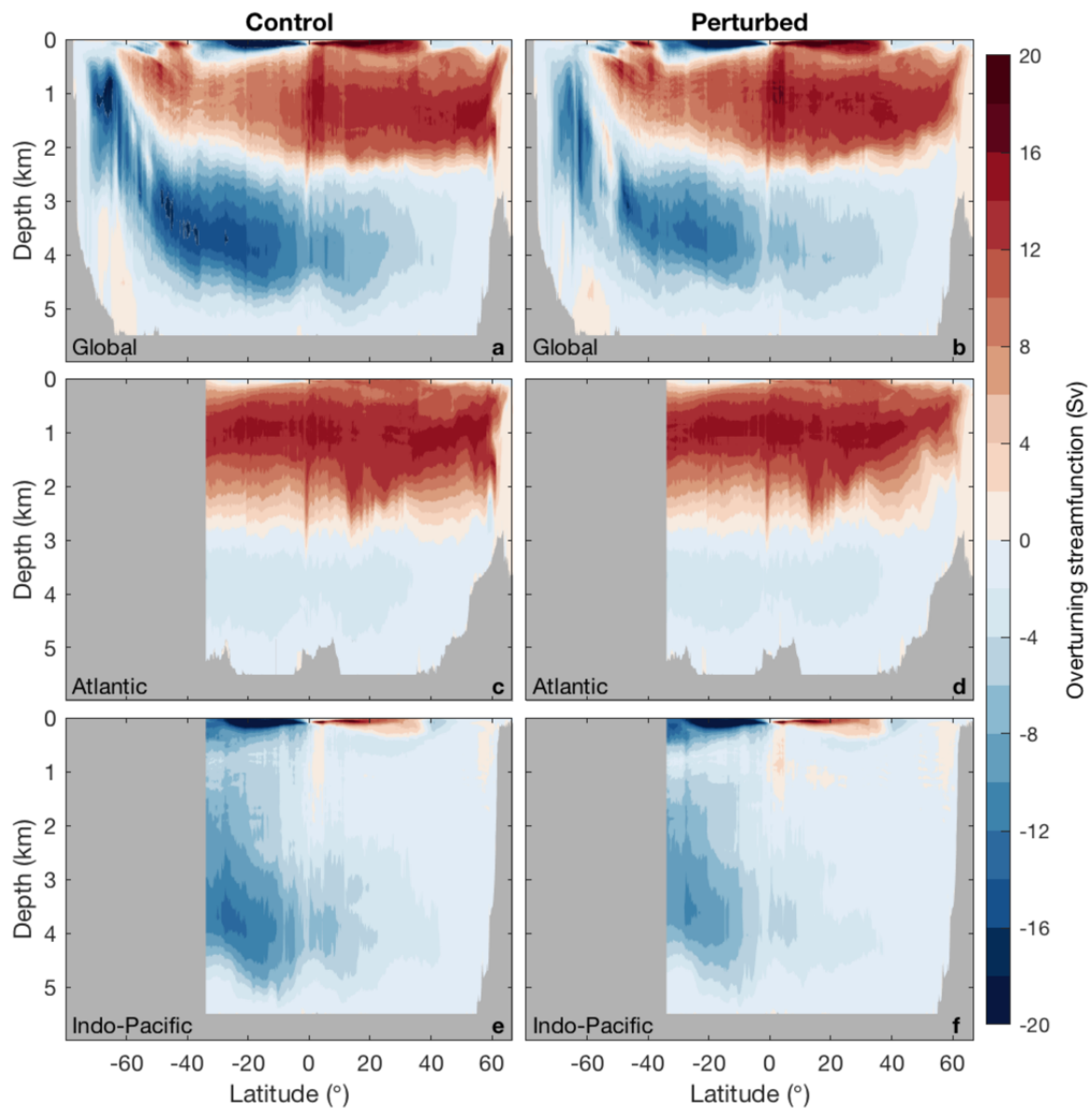
Fig. S6. MOM5-SIS-Wombat circulation results. (a-f) Meridional overturning streamfunction in the Control (a,c,e) and Perturbed experiments (b,d,f), for the global ocean (a,b), Atlantic ocean (c,d) and Indian-Pacific oceans (e,f). The streamfunction includes both resolved and parameterised advection. It is calculated in neutral density (Jackett & McDougall, 1997) coordinate and reprojected onto the depth coordinate (Zika et al., 2013) in order to eliminate adiabatic recirculations and avoid spurious effects due to vertical inversions in potential density fields.
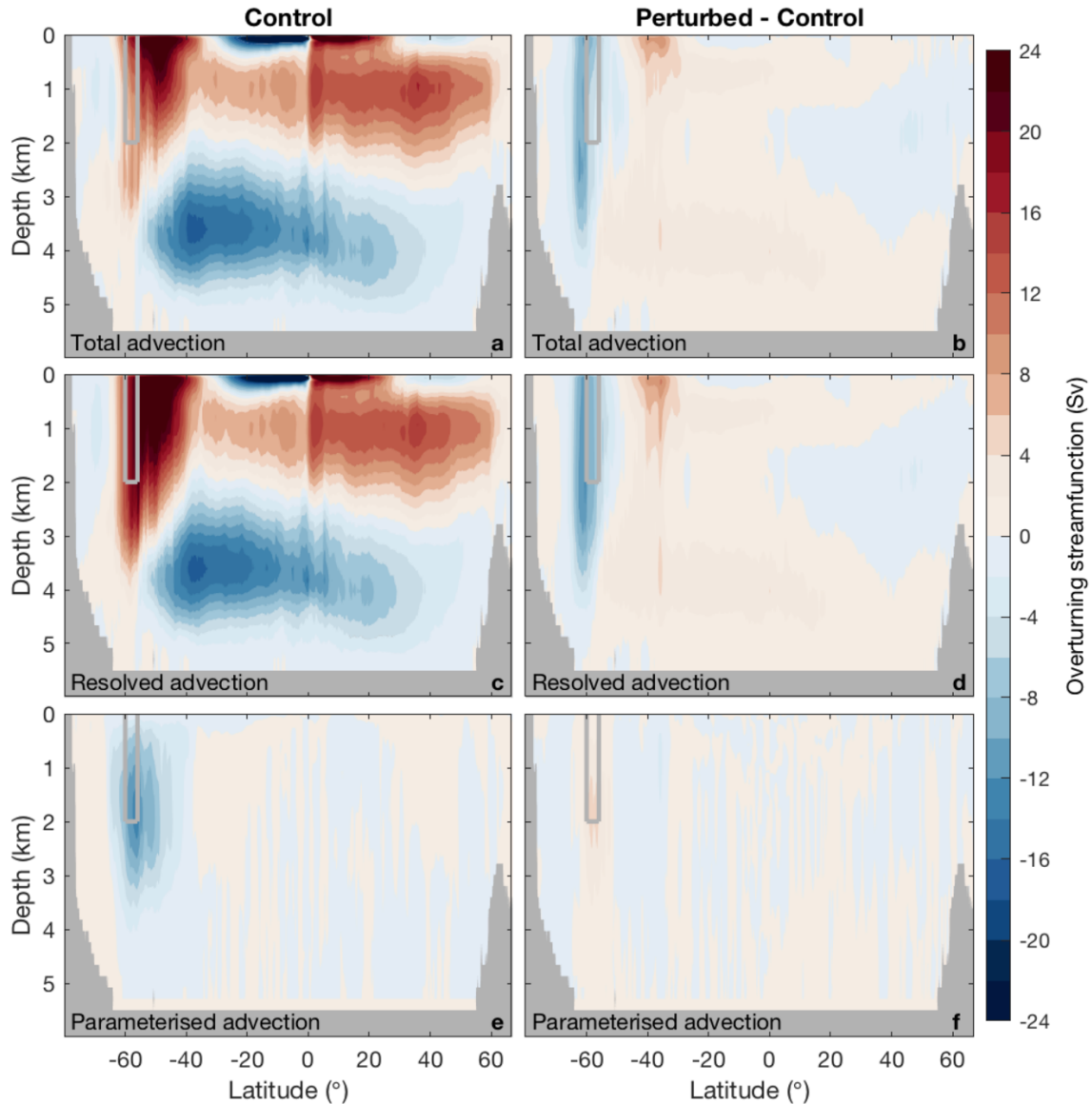
Fig. S7. Contributions to the overturning and its response. **(a,c,e)** Global overturning streamfunction averaged over the last decade of the Control experiment. The total, shown in (a), is decomposed into contributions of resolved advection (c) and of the eddy parameterisation (e). **(b,d,f)** Global overturning streamfunction anomaly (Perturbed minus Control) averaged over the last decade of the experiments. The total anomaly, shown in (b), is decomposed into the contributions of resolved advection (d) and of the eddy parameterisation (f). In all panels, the grey box illustrates the location of Drake Passage. Note that the absence of connection to the surface of the abyssal cell in (a) is an artefact of computing the overturning in depth (rather than density) space (cf Fig. S6).
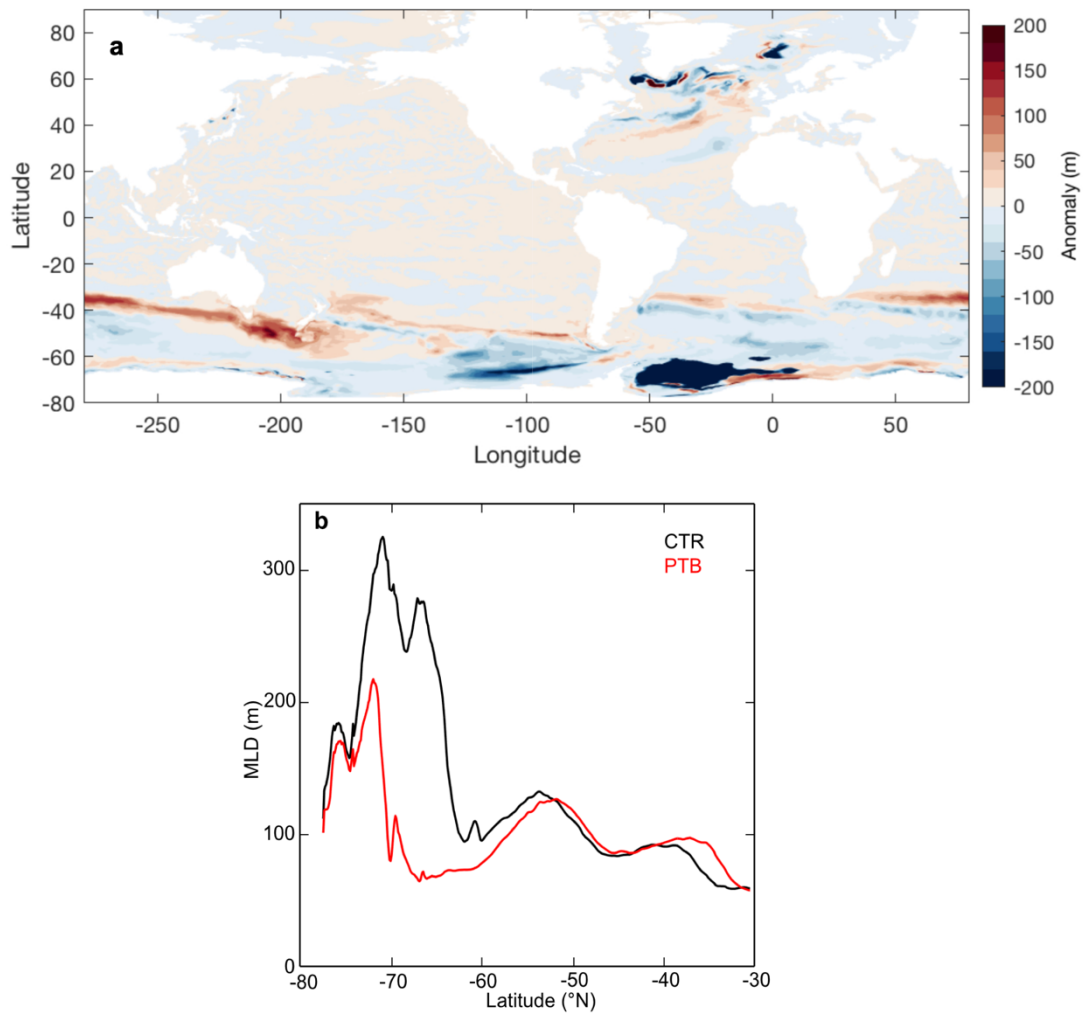
Fig. S8. MOM5-SIS-Wombat MLD results. (a) mixed layer depth (MLD) anomaly (perturbation-Control) **(b)** Zonally averaged mixed layer MLD in the Control (black) and Perturbed (red) simulations. Shown quantities are averaged over years 116-125 of each experiment.

Supporting Information References

Akhoudas, C. H., Sallée, J.-B., Reverdin, G., Haumann, F. A., Pauthenet, E., Chapman, C. C., Margirier, F., Lo Monaco, C., Metzl, N., Meilland, J., & Stranne, C. (2023). Isotopic evidence for an intensified hydrological cycle in the Indian sector of the Southern Ocean. *Nature Communications*, *14*(1), 2763. https://doi.org/10.1038/s41467-023-38425-5

Boyer, T. P., Antonov, J. I., Baranova, O. K., Garcia, H. E., Johnson, D. R., Mishonov, A. V., O'Brien, T. D., Seidov, D., I. (Igor), S., Zweng, M. M., Paver, C. R., Locarnini, R. A., Reagan, J. R., Coleman, C., & Grodsky, A. (2013). *World ocean database 2013.* https://doi.org/10.7289/V5NZ85MT

Gray, W. R., Wills, R. C. J., Rae, J. W. B., Burke, A., Ivanovic, R. F., Roberts, W. H. G., Ferreira, D., & Valdes, P. J. (2020). Wind-Driven Evolution of the North Pacific Subpolar Gyre Over the Last Deglaciation. *Geophysical Research Letters*, *47*(6), e2019GL086328. https://doi.org/10.1029/2019GL086328

Jackett, D., & McDougall, T. (1997). *A Neutral Density Variable for the World's Oceans*. https://doi.org/10.1175/1520-0485(1997)027<0237:ANDVFT>2.0.CO;2

Kalnay, E., Kanamitsu, M., Kistler, R., Collins, W., Deaven, D., Gandin, L., Iredell, M., Saha, S., White, G., Woollen, J., Zhu, Y., Chelliah, M., Ebisuzaki, W., Higgins, W., Janowiak, J., Mo, K. C., Ropelewski, C., Wang, J., Leetmaa, A., … Joseph, D. (1996). The NCEP/NCAR 40-Year Reanalysis Project. *Bulletin of the American Meteorological Society*, *77*(3), 437–472. https://doi.org/10.1175/1520-0477(1996)077<0437:TNYRP>2.0.CO;2

Kim, S.-T., & O'Neil, J. R. (1997). Equilibrium and nonequilibrium oxygen isotope effects in synthetic carbonates. *Geochimica et Cosmochimica Acta*, *61*(16), 3461–3475. https://doi.org/10.1016/S0016-7037(97)00169-5

LeGrande, A. N., & Schmidt, G. A. (2006). Global gridded data set of the oxygen isotopic composition in seawater. *Geophysical Research Letters*, *33*(12), L12604. https://doi.org/10.1029/2006GL026011

Lombard, F., Labeyrie, L., Michel, E., Bopp, L., Cortijo, E., Retailleau, S., Howa, H., & Jorissen, F. (2011). Modelling planktic foraminifer growth and distribution using an ecophysiological multi-species approach. *Biogeosciences*, *8*(4), 853–873. https://doi.org/10.5194/bg-8-853-2011

Paren, J. G., & Potter, J. R. (1984). Isotopic tracers in polar seas and glacier ice. *Journal of Geophysical Research*, *89*(C1), 749. https://doi.org/10.1029/JC089iC01p00749

Siler, N., Roe, G. H., & Armour, K. C. (2018). Insights into the Zonal-Mean Response of the Hydrologic Cycle to Global Warming from a Diffusive Energy Balance Model. *Journal of Climate*, *31*(18), 7481–7493. https://doi.org/10.1175/JCLI-D-18-0081.1

Strain, P. M., & Tan, F. C. (1993). Seasonal evolution of oxygen isotope-salinity relationships in high-latitude surface waters. *Journal of Geophysical Research*, *98*(C8), 14589. https://doi.org/10.1029/93JC01182

Zika, J. D., Le Sommer, J., Dufour, C. O., Molines, J.-M., Barnier, B., Brasseur, P., Dussin, R., Penduff, T., Iudicone, D., Lenton, A., Madec, G., Mathiot, P., Orr, J., Shuckburgh, E., & Vivier, F. (2013). Vertical Eddy Fluxes in the Southern Ocean. *Journal of Physical Oceanography*, *43*(5), 941–955. https://doi.org/10.1175/JPO-D-12-0178.1